Chinese Chemical Letters 36 (2025) 110314

Contents lists available at ScienceDirect

Chinese Chemical Letters

journal homepage: www.elsevier.com/locate/cclet

H_2S and NIR light-driven nanomotors induce disulfidptosis for targeted anticancer therapy by enhancing disruption of tumor metabolic symbiosis

Shangqian Zhang, Jiaxuan Li, Xuan Hu, Zelong Chen, Junliang Dong, Chenhao Hu, Shuang Chao, Yinghua Lv, Yuxin Pei*, Zhichao Pei*

College of Chemistry & Pharmacy, Northwest A&F University, Yangling 712100, China

ARTICLE INFO

Article history:
Received 4 May 2024
Revised 29 July 2024
Accepted 31 July 2024
Available online 2 August 2024

Keywords:
H_2S
NIR light
Nanomotors
Disulfidptosis
Tumor metabolic symbiosis

ABSTRACT

Disulfidptosis, a novel mechanism of programmed cell death through the disruption of tumor metabolic symbiosis (TMS), has showed tremendous potential in cancer therapy. However, the efficacy of disulfidptosis is limited by poor permeability of drugs in solid tumors. Herein, hydrogen sulfide (H_2S) and near-infrared (NIR) light-driven nanomotors (denoted as HGPP) have been constructed to efficiently penetrate tumors and induce disulfidptosis. HGPP demonstrate glutathione (GSH)-responsive release of H_2S, which combined with NIR light-induced photothermal effect drive HGPP movement to facilitate deep tumor penetration. The released H_2S induces tumor acidosis and disrupts TMS, where disulfide accumulation following cell starvation leads to disulfidptosis. In addition, HGPP induce hepatoma specific cellular uptake and catalyze the conversion of glucose and oxygen to produce hydrogen peroxide (H_2O_2), leading to glucose starvation. Overall, this study has developed a multifunctional Janus nanomotor that provides a novel strategy for disulfidptosis-based solid tumor therapy.

Tumor metabolic symbiosis (TMS), a typical feature that distinguishes tumor tissue from normal tissue, provides essential energy for cancer cells *via* metabolic heterogeneity, which enables cancer cells to be more adaptable to complex and variable environments [1-6]. Disruption of TMS can result in tumor cell death by interrupting its energy supply. TMS has therefore been recognized as a therapeutic target with great anti-cancer potential and attracted increasing interest in recent years [7,8]. However, the efficacy of cancer treatment by disrupting TMS is currently severely restricted by the poor penetration of existing therapeutic agents in solid tumors, especially cancer cells far from blood vessels, leading to an incomplete disruption [9,10]. Developing targeted drug delivery systems with deep tumor penetration is therefore urgently needed to achieve more extensive disruption of TMS and thus therapeutic success.

Among the various measures explored to tackle the challenge of solid tumor penetration, nanomotors hold great potential due to their high motility [11,12]. Their propulsion can be physical (magnetic field, ultrasound, light, and electric field), biological (sperm, algae, and fungi), and chemical (bubble, self-diffusion swimming, and self-electrophoresis) [13-22]. Notably, gas signaling molecules, such as carbon monoxide (CO), nitric oxide (NO), and hydrogen sulfide (H_2S), not only can drive nanomotors to facilitate penetration, but also provide beneficial therapeutic effects [23-25]. For example, NO in NO-driven nanomotors can promote revascularization and anti-tumor effect [26]. In addition, H_2S in H_2S-driven nanomotors, made of zwitterionic polymer nanoparticles loading L-cysteine, can induce acidosis and apoptosis of cancer cells by increasing glucose uptake and lactic acid production while inhibiting the efflux of lactic acid and protons. Moreover, these H_2S properties also disrupt TMS to further enhance anti-cancer efficacy. Therefore, rational design of nanomotors combining drug deep penetration and TMS disruption should be possible and of great significance.

In recent years, new programmed cell death mechanisms (such as ferroptosis and cuproptosis) have been discovered and attracted much attention from the cancer research community in the pursuit of new therapeutic strategies [27-30]. Very recently, Gan *et al.* found that aberrant accumulation of intracellular disulfides in cancer cells, caused by depletion of intracellular nicotinamide adenine dinucleotide phosphate (NADPH) under glucose starvation (a metabolic-stress condition), induces cell death. This new dis-

* Corresponding authors.
E-mail addresses: peiyx@nwafu.edu.cn (Y. Pei), peizc@nwafu.edu.cn (Z. Pei).

https://doi.org/10.1016/j.cclet.2024.110314
1001-8417/

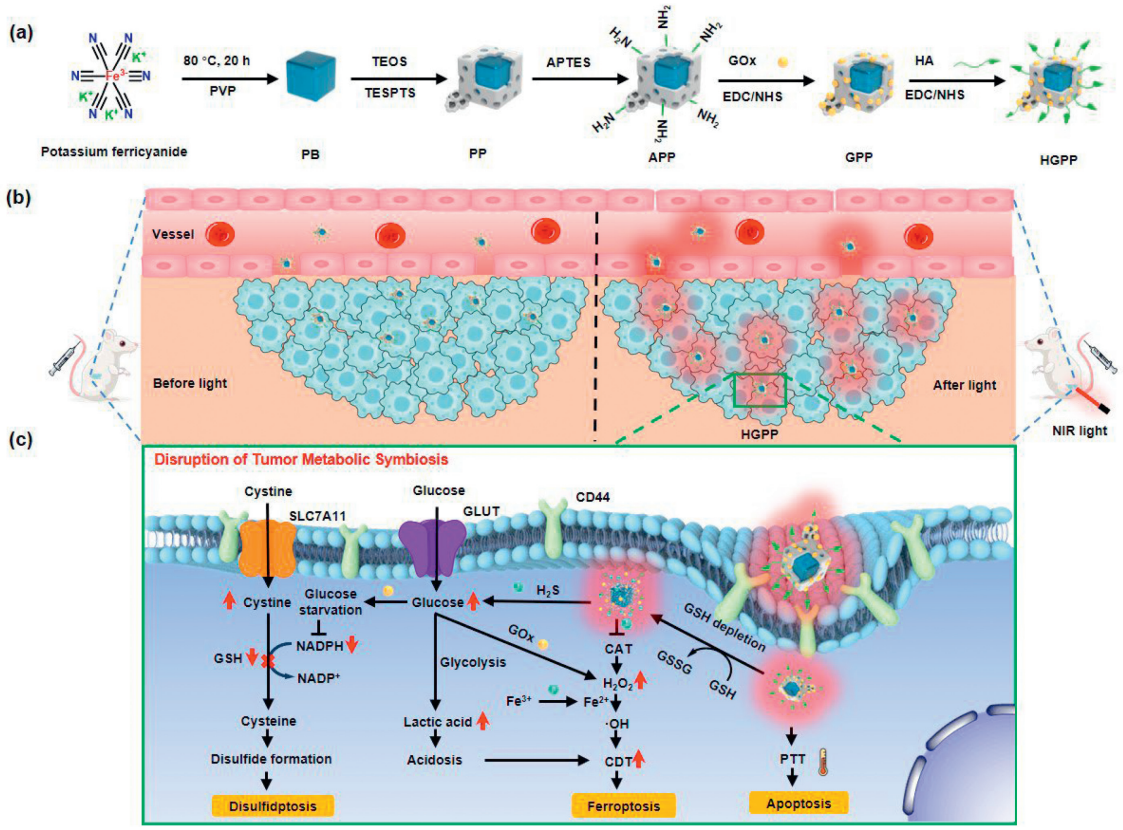

Scheme 1. Schematic illustration of (a) HGPP nanomotors synthetic process, (b) movement of HGPP nanomotors in tumor tissue without light on the left and with light on the right, and (c) TMS disruption mechanism. PB: Prussian blue nanoparticles; PP: PB@PMO; APP: APTES-PB@PMO; GPP: GOx-PB@PMO; HGPP: HA-GOx-PB@PMO.

tinct mechanism, termed by the authors as disulfidptosis [31,32], has not only advanced our fundamental understanding of cellular homeostasis, but might also be an effective therapeutic strategy to treat cancers. In addition to inducing disulfidptosis, glucose starvation can also generate significant TMS disruption since glucose is an essential nutrient to cancer cells and a key substance in TMS [10]. Previous studies have shown that TMS disruption induces apoptosis and ferroptosis [5,10], but its induction of disulfidptosis has not been reported to date.

Given all the above, we envision that rational design of a nanomotor which combines tumor penetration and disruption of TMS may achieve effective inhibition of metabolically heterogeneous tumors by inducing multimodal cell death (Scheme 1). In this work, Janus nanomotor (HGPP) was fabricated by enwrapping Prussian blue nanoparticles (PB) with periodic mesoporous organosilica (PMO), followed by modification with glucose oxidase (GOx) and hyaluronic acid (HA). For motility, PMO is decomposed by high concentration of glutathione (GSH) to produce H_2S, which together with the photothermal effect generated by PB with near infrared (NIR) light drives the movement of HGPP for enhanced tumor penetration. For TMS disruption, the HA modification improves hepatocellular carcinoma cell internalization, H_2S promotes glucose uptake, increases lactic acid production, and induces acidosis, while GOx decomposes glucose to produce H_2O_2 and gluconic acid, reduces adenosine triphosphate (ATP) production, and starves cancer cells. Moreover, disulfide accumulation following cell starvation also leads to disulfidptosis. This strategy of H_2S and NIR driven nanomotor shows great potential in cancer treatment by promoting drug penetration and enhancing TMS disruption.

HGPP was synthesized as per Scheme 1. The morphological characteristics and particle size of PB, PP, and HGPP were examined using transmission electron microscope (TEM) (Figs. 1a–c). PB displayed a uniform and smooth cubical structure with good dispersion and exhibited an average particle size of ~100 nm. PP displayed a coarse and Janus structure with an average particle size of ~200 nm. HGPP displayed a smooth surface with an average particle size of ~250 nm. Dynamic light scattering (DLS) results further confirmed the differences in particle size (Fig. S1a in Supporting information). During HGPP synthesis, double reversal of the nanoparticle zeta potential was also observed (Fig. S1b in Supporting information). Initially, the potential shifted from −22.8 mV of PP to 19.7 mV of APP, before reversing to −22.7 mV of GPP and −26.5 mV of HGPP. This phenomenon can be attributed to the surface charge alterations in the nanoparticle, which were first induced by the positive charge of APTES on the APP surface and subsequently by the negative charge of GOx on the GPP surface. Using ultraviolet–visible (UV–vis) spectroscopy, PB showed an absorption peak at 727 nm, while PP blue-shifted to 700 nm (Fig. S1c in Supporting information) The energy-dispersive spectrometry (EDS) mapping indicated a homogeneous distribution of Si, Fe, K, and N atoms throughout the HGPP (Fig. S2 in Supporting information). This indicates that HGPP successfully prepared [33,34]. X-ray photoelectron spectroscopy (XPS) was also utilized to characterize the elemental composition of HGPP (Fig. 1d), which showed obvious Fe 2p, O 1s, N 1s, C 1s, S 2p, and Si 2p signals. Similarly, Fourier transform infrared (FT-IR) spectrum of PP displayed the Si-O-Si vibration peak at 1080 cm^{-1} and -C=O stretching vibration peak at 1631 cm^{-1}, which indicated that the organosilicon layer was successfully covered onto the PB surface (Fig. S3 in Supporting information). The thermal gravimetric analysis (TGA) curve of HGPP is lower than (9.1%) GPP at 800 °C (Fig. 1e), reflecting the successful engraftment of HA to the GPP surface [35,36].

Previous studies have shown that tetra-sulfide bonds can be reduced by GSH to generate H_2S gas, which can be visually detected

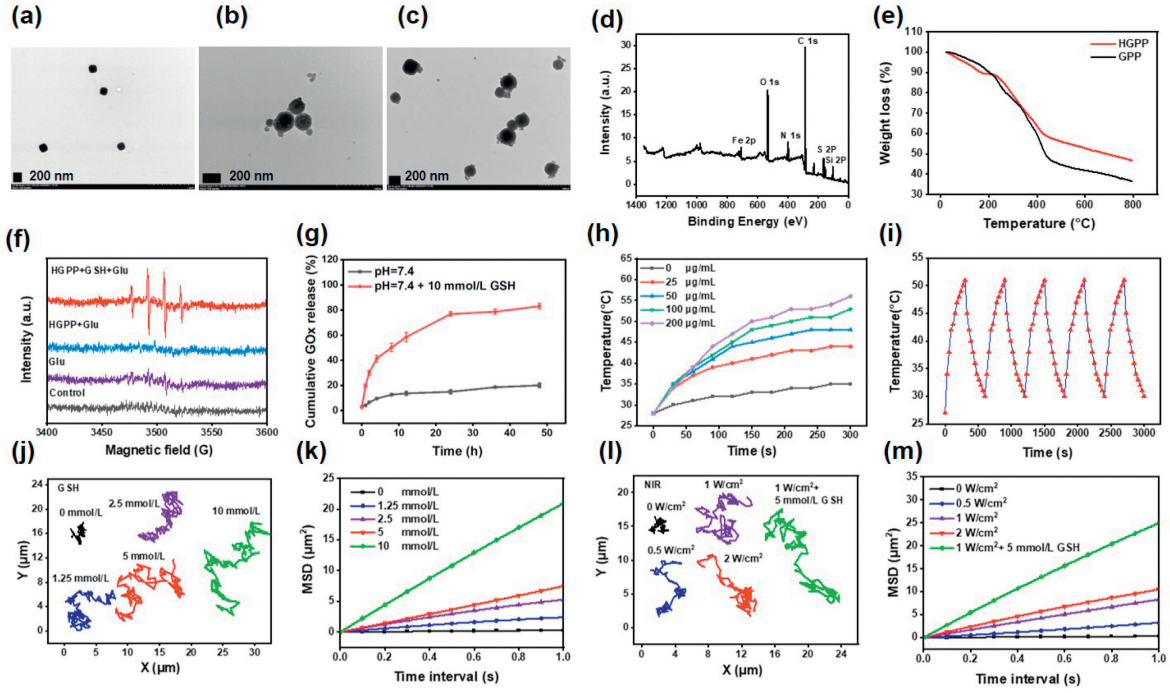

Fig. 1. TEM images of (a) PB, (b) PP, (c) HGPP. Scale bar: 200 nm. (d) XPS survey scan of HGPP. (e) TGA curves of GPP and HGPP. (f) Generation of ·OH in different samples. (g) Accumulated release curves of GOx in HGPP under different conditions. Data are presented as mean ± standard deviation (SD) ($n = 3$). (h) Photothermal curves of HGPP solution with different concentrations (808 nm, 1 W/cm^2). (i) Photothermal stability of HGPP solution (100 μg/mL) for five cycles under NIR light (808 nm, 1 W/cm^2). (j) Representative tracking trajectories of HGPP at different GSH concentrations ($n = 20$). (k) Correspondent mean square displacement (MSD) plots of HGPP at different GSH concentrations. (l) Representative tracking trajectories of HGPP under different NIR light power and under both NIR light and GSH ($n = 20$). (m) Correspondent MSD plots of HGPP under different NIR power and under both NIR light and GSH.

using $Pb(NO_3)_2$ test paper, as it reacts to form the black precipitate PbS [37,38]. The reaction process is presented as follows:

$$-S-S-S-S- + GSH \rightarrow GSSG + H_2S \quad (1)$$

$$Pb^{2+} + H_2S \rightarrow PbS\ (black) \quad (2)$$

To prove the ability of PMO in HGPP to consume GSH, a reduced GSH assay kit was used, which showed that GSH decreased with increasing HGPP concentration, decreasing to 30.06% of the control group at 200 μg/mL (Fig. S4a in Supporting information). Subsequently, $Pb(NO_3)_2$ test paper was used to prove the formation of H_2S from this reaction, where the paper became increasingly darker with reaction time (Fig. S4b in Supporting information). DMPD·2HCl can react with H_2S to form methylene blue (MB), which has an absorption at 660 nm (Figs. S5a and b in Supporting information). To quantify H_2S generation, HGPP was dispersed in GSH aqueous solution to produce H_2S for different durations (6, 24, and 48 h). Following this, the supernatant was obtained by centrifugation and then added to a zinc acetate/sodium acetate mixture to obtain Na_2S. MB was formed by adding DMPD·2HCl. The absorbance at 660 nm was then measured according to the standard curve of Na_2S, where 1870 μmol/L of H_2S was shown to be released from HGPP reacting with GSH for 48 h (Figs. S5b and c in Supporting information).

Previous literature has reported that H_2S can inhibit catalase (CAT) and increase the concentration of intracellular H_2O_2 [9]. The higher concentration of H_2O_2, the more ·OH is produced by Fenton reaction. To verify the inhibitory effect of H_2S on CAT, a CAT activity assay kit was used, which showed that the CAT activity of HGPP treated group decreased to 37.16% of the control group (Fig. S6 in Supporting information). Furthermore, the reduction of H_2S can convert Fe^{3+} into Fe^{2+}, thereby increasing Fenton catalytic activity. To assess the reduction potential of H_2S, XPS was used to evaluate the valence state change of Fe ions during the reaction between PB and sodium hydrosulfide (NaHS), which can be used as an H_2S donor to mimic H_2S [39,40]. Briefly, the binding energy of Fe 2p orbital in PB showed the peak area ratio of Fe^{2+}/Fe^{3+} to be 0.79 (Fig. S7a in Supporting information). After the reaction with NaHS, Fe^{3+} was reduced into Fe^{2+} and the peak area ratio of Fe^{2+}/Fe^{3+} increased to 0.93 (Fig. S7b in Supporting information), which suggests that H_2S can convert Fe^{3+} to Fe^{2+}.

The production of H_2O_2 in HGPP increases with the increase of glucose concentration, where the highest H_2O_2 production observed at a glucose concentration of 800 μg/mL is 82.26 μmol/L (Fig. S8a in Supporting information). To assess the ability of HGPP to produce H_2O_2 through GOx as well as enable Fenton catalysis, ·OH generation was detected using three methods, MB degradation, tetramethylbenzidine (TMB) oxidation, and electron spin resonance (ESR) spectroscopy [41,42]. MB is degraded by ·OH to form colorless small organic acids, leading to a decrease in the absorbance at 664 nm (Fig. S8b in Supporting information). When H_2O_2 was added to the reaction, the MB degradation rate was 8.3% for PB and 21% for PP. The higher rate observed in HGPP is a result of GSH consumption by the tetrasulfide bonds, which in turn reduced the ability of GSH to scavenge ·OH produced by Fenton reaction. In comparison, the MB degradation rate for HGPP without the addition of H_2O_2 was 53.8%, indicating significant H_2O_2 generation through GOx decomposing glucose. TMB oxidization was measured at 652 nm using UV–vis spectrometry (Fig. S8c in Supporting information). In the presence of glucose and GSH, the most oxidized TMB generated was in the HGPP group, indicating the highest amount of ·OH generation. To verify the generation of ·OH by HGPP, ESR spectra were recorded using 5,5-dimethyl-1-pyrroline *N*-oxide (DMPO) as a ·OH capture agent (Fig. 1f). In the HGPP with GSH and glucose condition, a 1:2:2:1 ·OH peak was observed, indicating ·OH production.

To determine the loading capacity (LC) of GOx in HGPP, quantification was carried out using fluorescence spectroscopy, which calculated the LC to be 1.01% (Fig. S9 in Supporting information). To investigate GSH-triggered release of GOx, HGPP was subjected to GSH (10 mmol/L) in phosphate buffered saline (PBS, pH 7.4) as well as PBS (pH 7.4) only, and the GOx release curves were plotted and compared against a standard curve based on the fluorescence spectra of different GOx concentrations (Fig. S9 in Supporting information). As shown in Fig. 1g, only a small amount of GOx leakage was observed under PBS (pH 7.4) only. However, in the presence of 10 mmol/L GSH, which simulates the high intracellular GSH levels of tumor cells, GOx was gradually released over time, reaching a maximum release of 83.1% within 48 h. This demonstrated that HGPP exhibits excellent GSH responsiveness where PP serves as a nanocarrier with GSH-responsive properties, enabling controlled release of GOx at the tumor site. As shown in Fig. S10 (Supporting information) illustrates the GSH-responsive degradation of HGPP. With the incubation at pH 6.8 and 37 °C with GSH (5.0 mmol/L) for 6 h, as revealed by the TEM images.

The photothermal conversion efficiency (η) of HGPP was investigated by monitoring temperature variations under NIR light (η = 29.45%, Fig. S11 in Supporting information). The temperature of HGPP was concentration-dependent in the range of 0–200 μg/mL (Fig. 1h) and HGPP showed good temperature responses to NIR light irradiation. Furthermore, HGPP demonstrated photothermal stability, with heat-cooling curve remaining consistent over five cycles (Fig. 1i and Fig. S12 in Supporting information).

To investigate the motility of HGPP, the propulsion performance under single-mode conditions was first measured using confocal laser scanning microscope (CLSM). Theoretically, a high concentration of GSH (1–10 mmol/L) in the tumor microenvironment can catalyze the production of H_2S by PMO in HGPP. The H_2S-driven motion was therefore investigated at different GSH concentrations (0, 1.25, 2.5, 5, and 10 mmol/L). The directed motion of HGPP was observed to be strongly dependent on GSH concentration, with increasing the concentration of GSH correlating strongly with enhanced particle diffusion coefficient MSD and velocity (Figs. 1j and k, Figs. S13 and S14a in Supporting information). This can be explained by H_2S being generated under localized chemical reactions between GSH and PMO on HGPP, and these Janus structural chemical reactions generate Janus chemical gradients around HGPP. This leads to the generation of forces in the direction from high to low product concentrations, triggering the directed self-propulsion towards the PB nanoshell side of the PMO. Under NIR light, HGPP was photoactivated and exhibited increasing MSD, velocity and moving distance with enhanced light power (Figs. 1l and m, Fig. S14b, and Motion video in Supporting information). This behavior can be attributed to heat generation of PB under NIR light irradiation and thermal asymmetry caused by the Janus structure of HGPP [43,44]. When HGPP was exposed to both light and chemical driving forces simultaneously, the directed motion was significantly greater than either force individually.

To examine the penetration ability of HGPP, a transwell migration experiment was conducted using fluorescein isothiocyanate (FITC)-HGPP [11]. In the transwell model, the upper and lower chambers were isolated and inoculated with HepG2 cells separately (Fig. 2a). FITC–HGPP were only incubated with HepG2 cells in the upper chamber. The fluorescence intensity of HepG2 cells in the lower chamber was then measured with CLSM to assess degree of penetration. As shown in Fig. 2b and Fig. S15 (Supporting information), HepG2 cells incubated with FITC–HGPP showed much stronger fluorescence intensity and thus better penetration into cancer cells compared with HepG2 cells incubated with FITC-PB, which lacks the self-driving nature of HGPP. This suggests that the motility of HGPP allows for deeper tumor penetration through intercellular infiltration [45-48].

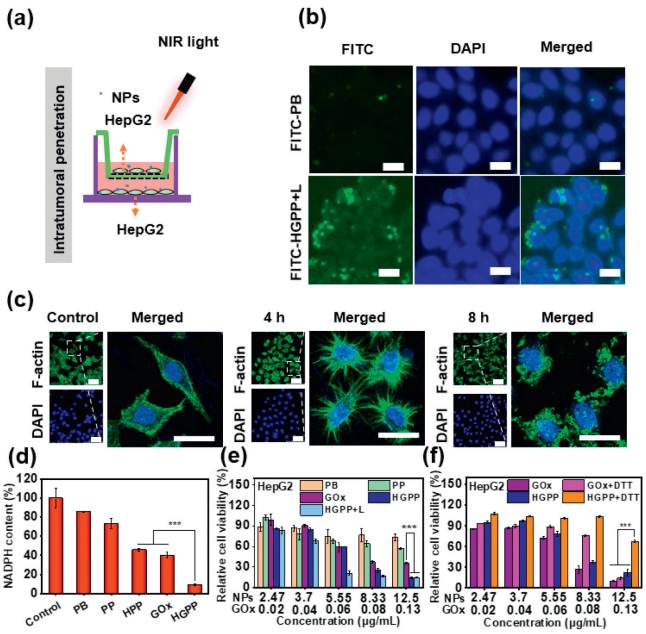

Fig. 2. (a) Schematic diagram of transwell model for nanomotors penetration. (b) CLSM diagram of cells in its lower chamber (scale bar: 40 μm). (c) Fluorescent staining of F-actin with FITC-phalloidin in HepG2 cells cultured with HGPP (8.33 μg/mL) for different durations (4, 8 h). Nuclei were stained by 4′,6-diamidino-2-phenylindole (DAPI). Scale bar: 50 μm. (d) Intracellular NADPH content after incubation with different samples (n = 3). The concentration of NPs is 8.33 μg/mL. (e) Cell viability of HepG2 cells, incubated with different samples for 24 h (n = 6, 808 nm, 1 W/cm^2). (f) Cell viability of HepG2 cells incubated with different samples with and without DTT for 24 h (n = 6). Data are presented as mean ± SD. $^{***}P < 0.001$.

To further investigate the penetration ability of HGPP, three-dimensional multicellular tumor spheroids (MCTS) were constructed as an *in vitro* model of solid tumor [49]. As shown in Fig. S16 (Supporting information), after 8 h incubation, there was a weak fluorescence signal in the middle of MCTS incubated with FITC-PB, while obvious fluorescence was observed in the same position of MCTS treated with FITC–HGPP and FITC–HGPP + NIR light (FITC–HGPP + L). In terms of penetration depth, FITC-PB achieved very limited penetration, FITC–HGPP penetrated well to a depth of 60–80 μm, while FITC–HGPP + L achieved strong penetration even at 100 μm.

To evaluate the anti-tumor ability of PB, PP, HPP (HA-PP), and HGPP, continuous monitoring following incubation with MCTS was carried out (Fig. S17 in Supporting information). During 4 days of culture, the volume of MCTS in the control group continuously increased. In contrast, MCTS in the other groups gradually decomposed and lost their 3D structure, with MCTS incubated with HGPP + L displaying the strongest growth inhibition. All these results indicate that HGPP promotes penetration, accumulation, and destruction of tumor, in particularly when combined with NIR light. The occurrence of apoptosis was then investigated with flow cytometry (FCM) using Annexin V-FITC and propidine iodide (PI) staining protocols. As shown in Fig. S18 (Supporting information), the apoptosis rates of HepG2 cells induced by HGPP was 75.2%, which suggests that the death of HepG2 cells under HGPP treatment is partly mediated by apoptosis.

To verify disulfidptosis as a main mechanism of cell death induced by HGPP. Since, F-actin contraction and reduced NADPH content are characteristics of cell disulfidptosis [31,50], CLSM was used to detect cell morphological changes, where it was observed that with the increase in incubation time, F-actin in HepG2 cells contracted (Fig. 2c), leading to the breaking of the cytoskeleton. As

a control, F-actin contraction was not observed in cells of the PB and PP groups, whereas F-actin contraction was observed in cells of the GOx and HGPP groups. This suggests that F-actin contraction may be caused by GOx (Fig. S19 in Supporting information). In addition, NADPH content in HepG2 cells decreased by 90% after HGPP treatment (Fig. 2d).

To assess the cytotoxicity of HGPP *in vitro*, the relative cell viability of two cell lines (HL7702 and HepG2) after co-incubation with HGPP was investigated using MTT assay. The survival rate of HL7702 cells was 90.49% at 12.5 μg/mL of HGPP (0.13 μg/mL for GOx), indicating that HGPP had limited toxicity to HL7702 cells (Fig. S20 in Supporting information). In contrast, for HepG2 cells, lower relative cell viability was observed at higher doses in all samples, with the highest toxicity observed in the group treated with HGPP + L (808 nm, 1 W/cm^2, 5 min), where only 14.06% of the cells survived after 24 h of incubation with 12.5 μg/mL of HGPP (0.13 μg/mL of GOx) (Fig. 2e). Half maximal inhibitory concentration (IC_{50}) of HGPP + L was 4.03 μg/mL, indicating excellent cytotoxicity towards HepG2 cells. In addition, disulfide-reducing reagent dithiothreitol (DTT) was used to inhibit the accumulation of intracellular disulfide [31,32]. As shown in Fig. 2f, the average survival rate of HepG2 cells co-incubated at 12.5 μg/mL of HGPP increased from 22.59% to 67.68% after the addition of DTT (2 mmol/L), while IC_{50} increased from 5.99 μg/mL to 58.04 μg/mL, indicating that DTT prevented cell death. These results indicate that HGPP can effectively consume intracellular NADPH and weaken the antioxidant capacity of HepG2 cells to induce cell death *via* disulfidptosis.

In addition, evaluation on hemolysis of HGPP showed weak hemolytic activity at concentrations lower than 25 μg/mL, and less than 5% hemolysis was observed when the HGPP concentration reached 25 μg/mL (Fig. S21 in Supporting information), indicating that HGPP has good biocompatibility and can be used for *in vivo* studies.

To assess the photothermal imaging potential of HGPP *in vivo*, HGPP solution was injected into BALB/c mice bearing H22 tumor through the tail vein. Subsequently, *in vivo* NIR (808 nm) photothermal imaging was performed at different time points. It was observed that the photothermal temperature peaked at the tumor site 16 h post-injection, suggesting maximum accumulation of HGPP at the tumor location (Fig. S22a in Supporting information). Thus, subsequent *in vivo* photothermal imaging of the tumor tissue was conducted at 16 h post injection. Tumor temperature was found to increase with NIR light (808 nm, 1.0 W/cm^2) duration across HGPP groups. Upon 5 min of NIR light irradiation, the tumor temperatures rose to 39.5 °C in the control and 46.0 °C in the HGPP group (Figs. S22b, c, and S23 in Supporting information). The average temperature of HGPP-treated tumors increased less than traditional photothermal treatment temperatures (≥50 °C) and could potentially reduce the side effects on normal tissues. HGPP therefore demonstrates promising photothermal imaging attributes *in vivo*, providing the foundation for an integrated diagnostic and therapeutic approach.

Moreover, an *in vivo* imaging system was utilized to examine the distribution of the 1,1′-dioctadecyl-3,3,3′,3′-tetramethylindodicarbocyanine, 4-chlorobenzenesulfonate salt (DID)-HGPP in H22 tumor-bearing mice at various time points following tail vein injection. The fluorescence intensity of DID at the tumor site exhibited a gradual increase, culminating in a peak around 16 h post-administration, and remained detectable even after 36 h (Fig. S24a in Supporting information). At 4 and 16 h following intravenous administration, the tumor and main organs were extracted to evaluate the fluorescence emitted by DID. DID-HGPP exhibited the highest mean fluorescence intensity in tumors 16 h after intravenous injection (Fig. S24b in Supporting information). All animal procedures complied with all relevant ethical regulations and were approved by the Northwest A&F University Animal Care Committee (NWAFU-314020038).

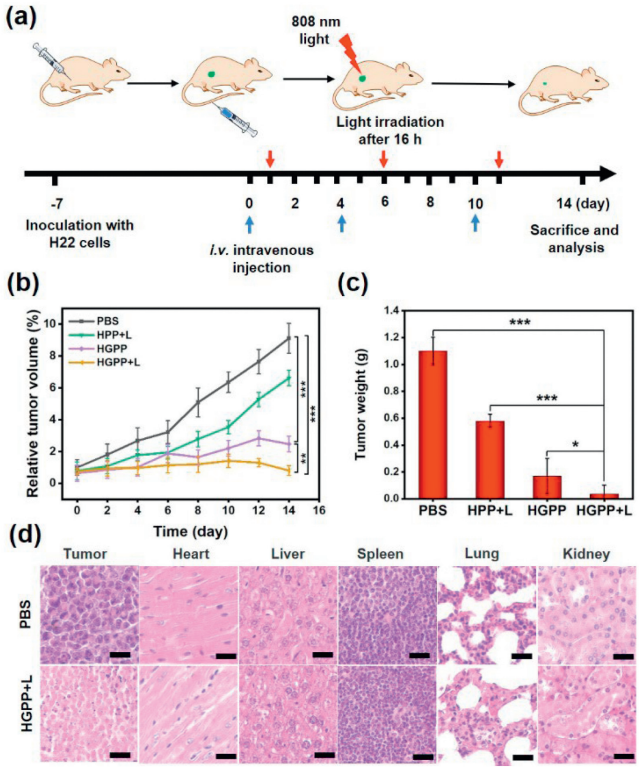

Fig. 3. (a) *In vivo* tumor therapeutic process. (b) Tumor growth curve over time in different treatment groups (the dosage of NPs administered is 5 mg/kg, 808 nm, 1 W/cm^2). (c) Tumor weight of mice in different treatment groups. (d) H&E staining of tumor and major organs 14 days after treatment. Scale bar: 50 μm. Data are presented as mean ± SD ($n = 6$). $^*P < 0.05$, $^{**}P < 0.01$, $^{***}P < 0.001$.

Given the encouraging *in vitro* results, *in vivo* anti-cancer efficacy of HGPP was investigated using BALB/c mice bearing H22 tumor [51-54]. After the tumor grew to 100–200 mm^3, mice were divided randomly into four groups (PBS, HPP + L, HGPP, and HGPP + L, $n = 6$) to receive treatments at a dose of 5 mg/kg once every four days. 16 h after administration, mice in HPP + L and HGPP + L groups were locally irradiated with an 808 nm light (Fig. 3a). Body weight and tumor volume were recorded every other day throughout the experiment to assess toxicity and tumor inhibition rates. As shown in Fig. 3b, Mice treated with HPP + L or HGPP showed incomplete inhibition of tumor growth. However, due to the synergistic effect of NIR and HGPP, mice treated with HGPP + L showed complete tumor growth inhibition. The mice were sacrificed on day 14, and the blood, organs, and tumors were collected. It can be found that the tumor inhibition effect of the HGPP+L group was significant, and the tumors disappeared in four of the mice (Fig. S25 in Supporting information). The tumor weight inhibition rate of HPP + L was 43.7%, compared with the control group. In contrast, the tumor weight inhibition rate of HGPP + L reached 92.0% indicating that HGPP + L has excellent anti-tumor efficacy *in vivo* (Fig. 3c and Fig. S26a in Supporting information). There was no weight loss in mice 14 days after tail vein injection with any of the solutions (Fig. S26b in Supporting information), while hematological parameters and blood biochemical analysis were almost unchanged after 14 days (Fig. S27 in Supporting information).

Furthermore, hematoxylin and eosin (H&E) staining was performed on all collected tumors and organs to evaluate the antitumor efficacy and acute toxicity of materials. No damage was detected in the organs of any group, indicating no significant acute

toxicity to normal tissues, while significant damage was observed at the tumor site in the HGPP + L group (Fig. 3d and Fig. S28 in Supporting information). TdT-mediated dUTP nick-end labeling (TUNEL) staining was performed to detect apoptotic tumor cells (Fig. S29 in Supporting information), where obvious tumor cell apoptosis was observed in HGPP + L group, when compared to the control group (PBS). These results indicate that HGPP + L not only has excellent ability to inhibit tumor growth, but also has good biocompatibility *in vivo*.

CLSM was used to investigate the tumor tissue penetration of HGPP + L. As shown in Fig. S30 (Supporting information), there was only a small amount of green fluorescence in FITC–HGPP treated tumor sections, most of which were concentrated at the edge of the tumor tissue. In contrast, FITC–HGPP + L showed excellent penetration ability, where green fluorescence could be observed in almost the entire tumor.

In summary, we have developed a novel nanomotor (HGPP) driven by NIR light and H_2S and applied it as an active drug delivery vehicle for enhanced tumor penetration and TMS disruption to induce disulfidptosis. HGPP exhibits excellent motility in tumors due to its Janus structure, ability to generate H_2S in the presence of GSH, and synergistic potential with photothermal effects. GOx-catalyzed conversion of glucose and oxygen to gluconic acid and H_2O_2 leads to starvation of cancer cells, where the reduction in NADPH and accumulation of disulfide induce disulfidptosis. *In vivo* experiments demonstrated that HGPP has good biocompatibility and anti-tumor activity, with a tumor inhibition rate of 92.0% in combination with NIR light. Therefore, HGPP successfully combines deep tumor penetration with TMS disruption to induces multimodal cell death and achieves effective inhibition of metabolically heterogeneous solid tumors, and thus holds significant potential in anti-cancer therapy.

Declaration of competing interest

The authors declare that they have no known competing financial interests or personal relationships that could have appeared to influence the work reported in this paper.

CRediT authorship contribution statement

Shangqian Zhang: Writing – original draft, Visualization, Methodology, Formal analysis, Data curation, Conceptualization. **Jiaxuan Li:** Project administration, Methodology, Investigation. **Xuan Hu:** Methodology, Investigation. **Zelong Chen:** Methodology, Investigation. **Junliang Dong:** Methodology, Investigation. **Chenhao Hu:** Methodology, Investigation. **Shuang Chao:** Methodology, Investigation. **Yinghua Lv:** Project administration, Investigation. **Yuxin Pei:** Writing – review & editing, Supervision, Resources, Funding acquisition. **Zhichao Pei:** Writing – review & editing, Supervision, Resources, Project administration, Funding acquisition.

Acknowledgments

This work was supported by the National Natural Science Foundation of China (No. 22171230) and the Project of Science and Technology of Social Development in Shaanxi Province (Nos. 2024SF-YBXM-294, 2023-YBSF-151). The authors thank the Teaching and Research Core Facility at College of Life Science, Life Science Research Core Services, Northwest A&F University for characterizations. The authors would like to thank Yihan Pei (Clare College, Cambridge) for language help.

Supplementary materials

Supplementary material associated with this article can be found, in the online version, at doi:10.1016/j.cclet.2024.110314.

References

[1] K.G. De La Cruz-López, L.J. Castro-Muñoz, D.O. Reyes-Hernández, et al., Front. Oncol. 9 (2019) 1143.
[2] U. Martinez-Outschoorn, F. Sotgia, M.P. Lisanti, Semin. Oncol. 41 (2014) 195–216.
[3] C.J. Halbrook, G. Thurston, S. Boyer, et al., Nat. Cancer 3 (2022) 1386–1403.
[4] J.M. Curry, M. Tuluc, D. Whitaker-Menezes, et al., Cell Cycle 12 (2013) 1371–1384.
[5] M. Wan, Z. Liu, T. Li, et al., Angew. Chem. Int. Ed. 60 (2021) 16139–16148.
[6] S. Hui, J.M. Ghergurovich, R.J. Morscher, et al., Nature 551 (2017) 115–118.
[7] H. Xiong, X. Liu, Z. Xie, et al., Adv. Healthcare Mater. 11 (2022) 2102724.
[8] C. Corbet, E. Bastien, N. Draoui, et al., Nat. Commun. 9 (2018) 1208.
[9] J. Wang, Z. Sun, S. Wang, et al., J. Am. Chem. Soc. 144 (2022) 19884–19895.
[10] W. Wang, L. Zhang, Q. Deng, et al., Nano Today 42 (2022) 101331.
[11] M. Tang, J. Ni, Z. Yue, et al., Angew. Chem. Int. Ed. 63 (2024) e202315031.
[12] J. Gao, H. Qin, F. Wang, et al., Nat. Commun. 14 (2023) 4867.
[13] M. Pal, N. Somalwar, A. Singh, et al., Adv. Mater. 30 (2018) 1800429.
[14] M. Hansen-Bruhn, B. Esteban-Fernández de Ávila, M. Beltrán-Gastélum, et al., Angew. Chem. Int. Ed. 57 (2018) 2657–2661.
[15] S. Zhang, X. Liu, Y. Hao, et al., J. Colloid Interf. Sci. 650 (2023) 67–80.
[16] M. Liu, L. Chen, Z. Zhao, et al., J. Am. Chem. Soc. 144 (2022) 3892–3901.
[17] Y. Tu, F. Peng, D. Wilson, Adv. Mater. 29 (2017) 1701970.
[18] M. Wan, T. Li, H. Chen, et al., Angew. Chem. Int. Ed. 60 (2021) 13158–13176.
[19] R. Zhuang, D. Zhou, X. Chang, et al., Appl. Mater. Today 26 (2022) 101314.
[20] Q. Zhan, X. Shi, D. Fan, et al., Chem. Eng. J. 404 (2021) 126443.
[21] X. Chang, Y. Feng, B. Guo, et al., Nanoscale 14 (2022) 219–238.
[22] J. Li, C.C. Mayorga-Martinez, C.D. Ohl, et al., Adv. Funct. Mater. 32 (2022) 2102265.
[23] S.B. Wang, C. Zhang, Z.J. Chen, et al., ACS Nano 13 (2019) 5523–5532.
[24] N. Li, C. Huang, J. Zhang, et al., ACS Nano 17 (2023) 12573–12593.
[25] F. Tong, J. Liu, Y. Zhong, et al., Appl. Mater. Today 32 (2023) 101823.
[26] H. Chen, T. Shi, Y. Wang, et al., J. Am. Chem. Soc. 143 (2021) 12025–12037.
[27] Q. Fan, W. Xiong, H. Zhou, et al., Adv. Mater. 35 (2023) 2305932.
[28] S.J. Dixon, K.M. Lemberg, M.R. Lamprecht, et al., Cell 149 (2012) 1060–1072.
[29] L. Qiao, G. Zhu, T. Jiang, et al., Adv. Mater. 36 (2024) 2308241.
[30] F. Zhao, L. Liang, H. Wang, et al., Adv. Funct. Mater. 33 (2023) 2300941.
[31] X. Liu, L. Nie, Y. Zhang, et al., Nat. Cell Biol. 25 (2023) 404–414.
[32] Y. Yan, H. Teng, Q. Hang, et al., Nat. Commun. 14 (2023) 3673.
[33] L. Hou, X. Gong, J. Yang, et al., Adv. Mater. 34 (2022) 2200389.
[34] L. Fu, Y. Wan, C. Qi, et al., Adv. Mater. 33 (2021) 2006892.
[35] W. Tian, Y. Su, Y. Tian, et al., Adv. Sci. 4 (2017) 1600356.
[36] W. Xu, J. Qian, G. Hou, et al., Adv. Funct. Mater. 32 (2022) 2205013.
[37] Z.W. Lee, X.Y. Teo, E.Y.W. Tay, et al., Br. J. Pharmacol. 171 (2014) 4322–4336.
[38] B. Liu, S. Liang, Z. Wang, et al., Adv. Mater. 33 (2021) 2101223.
[39] J. Chen, F. Xue, W. Du, et al., Nano Lett. 22 (2022) 6156–6165.
[40] B. Li, Q. Li, Z. Qi, et al., Angew. Chem. Int. Ed. 63 (2024) e202316323.
[41] J. Liang, Y. Sun, K. Wang, et al., ACS Appl. Mater. Interfaces 15 (2023) 18191–18204.
[42] D. Ren, L. Tang, Z. Wu, et al., Chin. Chem. Lett. 34 (2023) 108617.
[43] J. Yu, Y. Li, A. Yan, et al., Adv. Sci. 10 (2023) 2301919.
[44] H. Liu, J. Zhang, Y. Jia, et al., Chem. Eng. J. 442 (2022) 135994.
[45] Y. Kang, W. Sun, S. Li, et al., Adv. Sci. 6 (2019) 1900716.
[46] S. Jeon, J. Clavadetscher, D.K. Lee, et al., Nanomaterials 8 (2018) 1028.
[47] S. Cao, Z. Pei, Y. Xu, et al., Chem. Mater. 28 (2016) 4501–4506.
[48] Y. Qu, W. Jin, Y. Wan, et al., Chin. Chem. Lett. 35 (2024) 108493.
[49] H. Lu, M.H. Stenzel, Small 14 (2018) 1702858.
[50] T. Sun, H. Wang, X. Zhang, et al., Small Struct. 5 (2023) 2300350.
[51] Z. Tang, S. Wu, P. Zhao, et al., Adv. Sci. 9 (2022) 2201232.
[52] B. Xie, H. Zhao, Y.F. Ding, et al., Adv. Sci. 10 (2023) 2304407.
[53] Z. Shen, N. Ma, F. Wang, et al., Chin. Chem. Lett. 33 (2022) 4563–4566.
[54] J. Liu, W. Zhang, X. Wang, et al., J. Am. Chem. Soc. 36 (2023) 19662–19675.